





Cite this: *RSC Adv.*, 2019, 9, 4150

# A highly selective and sensitive H<sub>2</sub>S sensor at low temperatures based on Cr-doped $\alpha$ -Fe<sub>2</sub>O<sub>3</sub> nanoparticles

Dongyang Xue,  Rui Zhou, Xiaoping Lin, Xiaochuan Duan,  Qihong Li\* and Taihong Wang

Cr-doped  $\alpha$ -Fe<sub>2</sub>O<sub>3</sub> nanoparticles were synthesized by a low-cost and environmentally friendly hydrothermal route. Their gas sensing properties were investigated and the sensor showed high sensitivity and selectivity to H<sub>2</sub>S gas. Different Cr doping levels from 0 to 8.0 wt% were studied, and the sensor of 4.0 wt% Cr-doped  $\alpha$ -Fe<sub>2</sub>O<sub>3</sub> showed the largest response, with a response of 213 to 50 ppm H<sub>2</sub>S at 100 °C. The incorporation of Cr ions within  $\alpha$ -Fe<sub>2</sub>O<sub>3</sub> nanocrystals increases the specific surface area, and promotes the oxidation of H<sub>2</sub>S and oxygen adsorption in the air. Thus, the doping of Cr into  $\alpha$ -Fe<sub>2</sub>O<sub>3</sub> nanostructures would be a promising method for designing and fabricating high performance H<sub>2</sub>S gas sensors.

Received 4th September 2018  
 Accepted 3rd January 2019

DOI: 10.1039/c8ra07365a

[rsc.li/rsc-advances](http://rsc.li/rsc-advances)

## 1. Introduction

Recently, atmospheric environmental pollution has become one of the most serious problems that all the countries of the earth are facing.<sup>1</sup> Many steps have been taken to resolve it, such as enhancing control over pollutant discharge, researching high-performance catalysts for the catalytic conversion of auto exhausts, developing new technologies for the monitoring of toxic gases, enhancing the environmental awareness of people *etc.* Among these, controlling and monitoring poisonous gases from sources of pollution are quite important so far. Accordingly, the development of gas sensors with enhanced sensitivity and selectivity is very urgent and important.

Hydrogen sulfide (H<sub>2</sub>S) is a colorless, highly flammable and extremely toxic gas with a characteristic foul odour of rotten eggs.<sup>2–5</sup> Furthermore, it is also produced in large quantity from industrial activities and places such as petroleum natural gas drilling and refining, wastewater treatment, coke ovens, tanneries, kraft paper mills, and landfills.<sup>6,7</sup> Hence, it is necessary to detect concentrations of H<sub>2</sub>S in work environments such as oil and natural gas industries. To date, much effort has been made to prepare a number of gas-sensing nanomaterials, such as Fe<sub>2</sub>O<sub>3</sub>,<sup>8–13</sup> WO<sub>3</sub>,<sup>14</sup> SnO<sub>2</sub>,<sup>15</sup> CuO,<sup>16</sup> ZnO,<sup>3</sup> and some compounds.<sup>17–19</sup> Among them,  $\alpha$ -Fe<sub>2</sub>O<sub>3</sub> is an excellent potential H<sub>2</sub>S-sensitive material.

In recent years,  $\alpha$ -Fe<sub>2</sub>O<sub>3</sub> has attracted great attention for its distinctive sensing properties toward H<sub>2</sub>S gas. Despite some exciting results obtained, the development of more highly

sensitive and markedly selective gas sensors based on  $\alpha$ -Fe<sub>2</sub>O<sub>3</sub> nanostructures remains a challenge. Up to now, many efforts have been taken such as heterostructure constructing, element doping, and decorating in order to improve its performance.<sup>10,20,21</sup> Among these methods, element doping has been turned out to be a very simple and feasible method. Chromium, as a member of transition metals, exhibits a wide range of possible oxidation states. And it is a promising candidate for efficient doping materials in sensor applications. There have been some reports showing the performance of Cr dopant in ammonia sensors,<sup>22–24</sup> NO<sub>2</sub> sensors,<sup>25,26</sup> acetone sensors,<sup>27</sup> oxygen sensor,<sup>28</sup> and so on. Herein we report a facile one-step hydrothermal method to synthesize Cr-doped  $\alpha$ -Fe<sub>2</sub>O<sub>3</sub> nanoparticles, for optimizing the gas sensing properties. At 100 °C, the sensor using 4 wt% Cr-doped  $\alpha$ -Fe<sub>2</sub>O<sub>3</sub> displayed the highest response toward hydrogen sulfide gases with a low cross-selectivity and short response time. The enhanced sensing response can be attributed to the increases in surface area and catalysis effect by Cr doping.

## 2. Experimental details

### 2.1 Synthesis of Cr-doped $\alpha$ -Fe<sub>2</sub>O<sub>3</sub>

All of the reagents used in the experiments were of analytical grade without further purification. Fe(NO<sub>3</sub>)<sub>3</sub>·9H<sub>2</sub>O and Cr(NO<sub>3</sub>)<sub>3</sub>·9H<sub>2</sub>O were used as iron and chromium sources, respectively. A series of Cr-doped  $\alpha$ -Fe<sub>2</sub>O<sub>3</sub> (0.0, 2.0, 4.0, 6.0, and 8.0 wt%) nanoparticles were synthesized by one-step hydrothermal reaction. In a typical experiment, Fe(NO<sub>3</sub>)<sub>3</sub>·9H<sub>2</sub>O (0.8077 g), Urea (0.5 g) and Cr(NO<sub>3</sub>)<sub>3</sub>·9H<sub>2</sub>O (0.0168 g) were put into 35 ml of distilled water to form homogeneous solution under vigorous stirring. Subsequently 300  $\mu$ l ammonia was

Pen-Tung Sah Institute of Micro-Nano Science and Technology, Xiamen University, Xiamen, China. E-mail: [liqihong@xmu.edu.cn](mailto:liqihong@xmu.edu.cn); Fax: +86-0592-2187196; Tel: +86-0592-2187198



introduced into above solution by magnetic stirring. The precursor solution was continuously stirred at room temperature to obtain a homogeneous mixture. Afterwards, the solution was transferred to a Teflon-lined stainless steel autoclave with a capacity of 50 ml and maintained at 180 °C for 12 h. After the hydrothermal procedure, the autoclave naturally cooled to room temperature. The solid products were subjected to centrifugation, rinsed alternately with distilled water and ethanol several times, and dried at 70 °C in air for 24 h. Finally, the dry precipitates were annealed in a muffle furnace at 500 °C for 2 h in air.

## 2.2 Sensor fabrication and sensing measurements

In a typical experiment, a small amount of the sensing material powder was mixed with terpineol followed by 2 h grinding to form a paste, then coated uniformly onto a ceramic tube. After the coating was air dried, the  $\alpha$ -Fe<sub>2</sub>O<sub>3</sub>-coated Al<sub>2</sub>O<sub>3</sub> microtube was fixed to a special pedestal with six poles by welding four Pt electrodes to four poles of the pedestal. A Ni–Cr heating coil was then inserted through the Al<sub>2</sub>O<sub>3</sub> microtube, and its two ends were welded to the other two poles of the pedestal. A schematic representation and a micrograph image of gas sensor were shown in Fig. 1. The measurements of hydrogen sulfide gases sensing were conducted on a ZhongKe NS-4003 Smart Sensor Analyser (Beijing ZhongKe Micro-Nano Networking Technology Co., Ltd.). The relative humidity at room temperature was about 52% during the whole experiment. The sensor response is defined as  $\text{response} = R_a/R_g$ , where  $R_a$  is the resistance in air and  $R_g$  is the measured resistance in the presence of the test gas. The response time is defined as the period in which the sensor output change reached 90% of the stabilized value, similarly, the recovery time is defined as the time required for the sensor to reach 10% of the initial steady-state value after the sensor was taken out of the test chamber.

## 2.3 Characterization

X-ray powder diffraction (XRD) data of the as synthesized materials were collected on a Philips X'pert pro diffractometer using Cu-K $\alpha$  radiation at 40 kV and 30 mA. Scanning electron microscopy (SEM) images and EDX data were recorded on a scanning electron microscope (SEM, Zeiss SUPRA 55) equipped with an energy dispersive X-ray Spectroscopy (EDS, Oxford).

The transmission electron microscopy images (TEM) were obtained using JEOL JEM-2100. The Raman spectra were performed by using the IDSpec ARCTIC Raman system. X-ray photoelectron spectroscopy (XPS) measurements were performed with a PHI Quantum 200 spectrophotometer with Mg K radiation.

# 3. Results and discussion

## 3.1 Characterization of sensor material

The Raman spectrum of the  $\alpha$ -Fe<sub>2</sub>O<sub>3</sub> is presented in Fig. 2. In the range of 200–1500 cm<sup>-1</sup>, many peaks could be observed, which were located at 225, 290, 405, 495, 611, 658, 825, 1081, and 1322 cm<sup>-1</sup>, respectively. All these peaks correspond to  $\alpha$ -Fe<sub>2</sub>O<sub>3</sub> phase.<sup>29,30</sup> The XRD patterns of the pure and Cr-doped  $\alpha$ -Fe<sub>2</sub>O<sub>3</sub> samples are shown in Fig. 3a. Clearly, all the diffraction peaks of all the samples could be indexed to the rhombohedral structure of  $\alpha$ -Fe<sub>2</sub>O<sub>3</sub> phase (JCPDS file no. 33-0664). No other peaks corresponding to Cr-related compounds were observed in all the XRD patterns of 0–8 wt% Cr-doped  $\alpha$ -Fe<sub>2</sub>O<sub>3</sub> samples. In addition, as shown in Fig. 3b, a high angle shift was detected from the (110) peak *via* comparing the different Cr doping  $\alpha$ -Fe<sub>2</sub>O<sub>3</sub>. This is due to larger ionic radius of Fe<sup>3+</sup> (0.67 Å) as compared to Cr<sup>3+</sup> (0.64 Å), which according to Bragg's law shifts the peak position to high diffraction angles. The incorporation

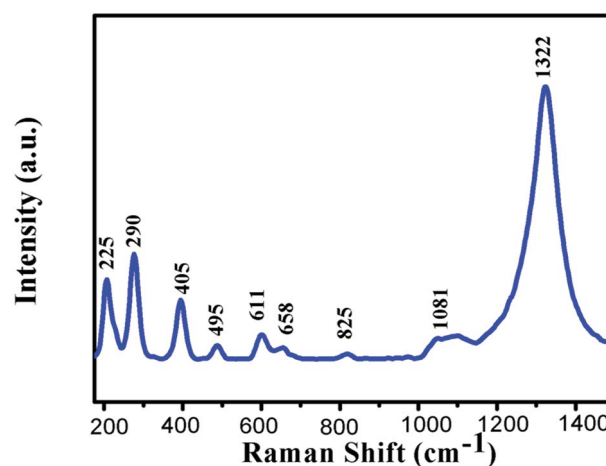


Fig. 2 Raman scattering spectra of pristine  $\alpha$ -Fe<sub>2</sub>O<sub>3</sub>.

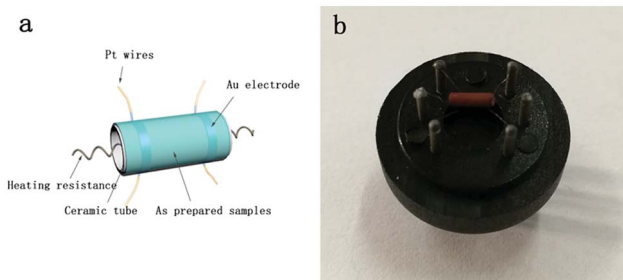


Fig. 1 (a) A schematic representation and (b) a micrograph image of gas sensor.

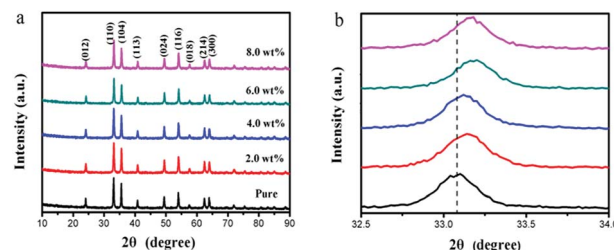


Fig. 3 (a) XRD patterns and (b) high-resolution of (110) peak of the pure, 2.0 wt%, 4.0 wt%, 6.0 wt% and 8.0 wt% Cr-doped  $\alpha$ -Fe<sub>2</sub>O<sub>3</sub> nanoparticles.



of atom with low ionic radius atom results in shrink of unit cell that decreases the lattice parameter and decreases *d*-spacing thus shifting peak positions to higher angles. Therefore, the substitution of Fe<sup>3+</sup> by Cr<sup>3+</sup> induced the high angle shift of diffraction peaks, suggesting that Cr element is incorporated into the  $\alpha$ -Fe<sub>2</sub>O<sub>3</sub> lattice.

Morphology of the pristine and Cr-doped  $\alpha$ -Fe<sub>2</sub>O<sub>3</sub> structures were also discerned by SEM observations. As shown in Fig. 4a, spherical particles coexisted with irregular particle aggregates. As the amount of Cr<sup>3+</sup> was increased to 4 wt%, the obtained product consisted of small nanospheres with good monodispersity, as shown in Fig. 4c. However, particle aggregates without an orderly shape were collected when the amount of Cr<sup>3+</sup> increased to 8 wt%, as shown in Fig. 4e.  $\alpha$ -Fe<sub>2</sub>O<sub>3</sub> nanoparticles can be obtained by using a one-step hydrothermal process at an appropriate concentration of ammonia. And Cr<sup>3+</sup> may control the morphology of  $\alpha$ -Fe<sub>2</sub>O<sub>3</sub> because of its acid nature.<sup>23,31</sup> The detailed mechanism of Cr on Fe<sub>2</sub>O<sub>3</sub> nanoparticle is not clear now and needs further study. The EDS patterns of 4 wt% Cr-doped  $\alpha$ -Fe<sub>2</sub>O<sub>3</sub> nanoparticles shown in Fig. 3f indicate that the as-prepared 4 wt% Cr-doped  $\alpha$ -Fe<sub>2</sub>O<sub>3</sub> nanoparticles are composed of Fe, O and Cr, where the *x*-axis represents X-ray energy (in keV) and the *y*-axis represents the intensity. And it is evident that the peaks associated with chromium in the doped samples confirm the presence of chromium in  $\alpha$ -Fe<sub>2</sub>O<sub>3</sub> nanoparticles.

Microstructures of the as-prepared products were studied by selected area electron diffraction (SAED) and high resolution transmission electron microscopy (HRTEM) characterizations. As shown in Fig. 5a, 4 wt% Cr-doped  $\alpha$ -Fe<sub>2</sub>O<sub>3</sub> nanoparticles were observed by low magnification transmission electron microscopy. In the HRTEM images shown in Fig. 5b and c, we found

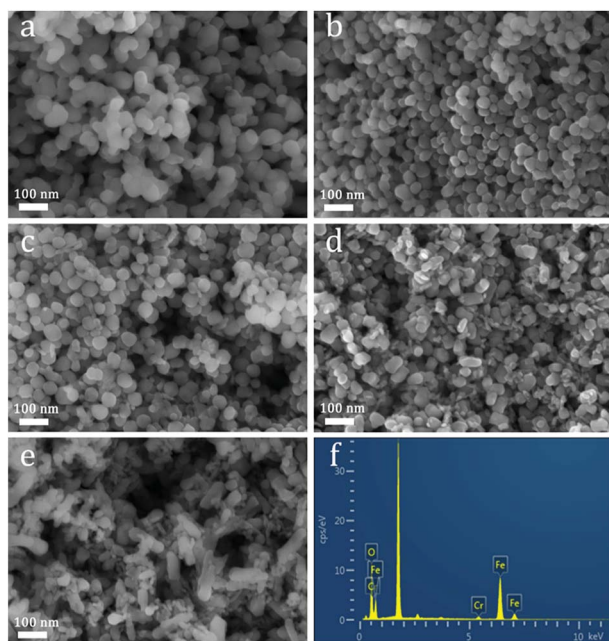


Fig. 4 (a–e) Typical SEM images of the pure, 2.0 wt%, 4.0 wt%, 6.0 wt% and 8.0 wt%  $\alpha$ -Fe<sub>2</sub>O<sub>3</sub> nanoparticles, (f) the EDX spectrum of the 4.0 wt%  $\alpha$ -Fe<sub>2</sub>O<sub>3</sub> nanoparticles.

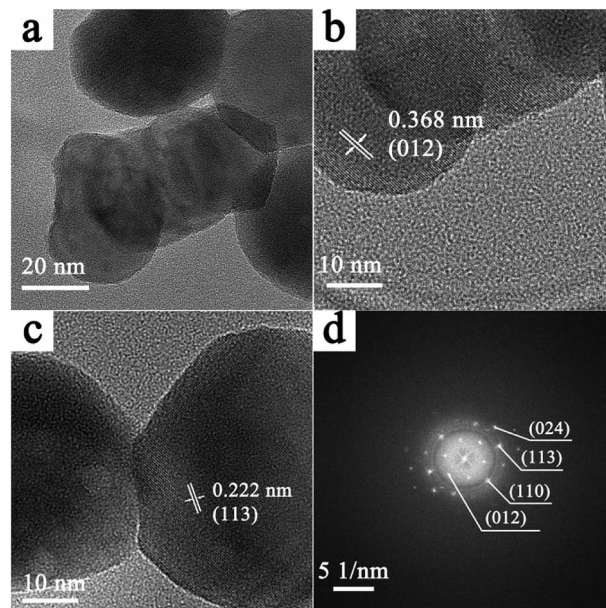


Fig. 5 (a) Low magnification TEM image of the 4 wt% Cr-doped  $\alpha$ -Fe<sub>2</sub>O<sub>3</sub>. (b and c) HRTEM images and (d) SAED pattern of the 4 wt% Cr-doped  $\alpha$ -Fe<sub>2</sub>O<sub>3</sub>.

the lattice distances were about 0.368 nm and 0.222 nm, which can be corresponded to the (012) and (113) lattice plane of  $\alpha$ -Fe<sub>2</sub>O<sub>3</sub>. The diffraction pots in a SAED pattern (Fig. 5d) matched well with (012), (110), (113) and (024) planes of  $\alpha$ -Fe<sub>2</sub>O<sub>3</sub>.

X-ray photoelectron spectroscopy (XPS) was performed to illuminate the surface composition of the studied 4 wt% Cr-doped  $\alpha$ -Fe<sub>2</sub>O<sub>3</sub> nanoparticles. The spectra of Fe 2p and Cr 2p are shown in Fig. 6. In Fig. 6a, the bending energies of Fe 2p<sub>3/2</sub> and Fe 2p<sub>1/2</sub> are 710.7 and 724.3 eV, respectively, which are in good agreement with the literature values of Fe<sup>3+</sup> in  $\alpha$ -Fe<sub>2</sub>O<sub>3</sub>.<sup>32–34</sup> The binding energy of Cr 2p<sub>3/2</sub> is 577.8 eV and Cr 2p<sub>3/2</sub>–Cr 2p<sub>1/2</sub> binding energy separation is 9.6 eV, that is typical for Cr<sup>3+</sup> centers dispersed in an oxide environment (Fig. 6b).<sup>35–37</sup>

## 3.2 Gas sensing properties

**3.2.1 Gas-sensing measurement.** Gas sensing experiments to 50 ppm hydrogen sulfide gases at different temperatures are performed as shown in Fig. 6a. The responses of pure, 2.0 wt%, 4.0 wt%, 6.0 wt%, and 8.0 wt% Cr-doped  $\alpha$ -Fe<sub>2</sub>O<sub>3</sub> samples are tested at the temperatures from 60 to 160 °C which are found to increase with the increasing temperature, reach the maximum at a certain temperature, and then decrease with a higher

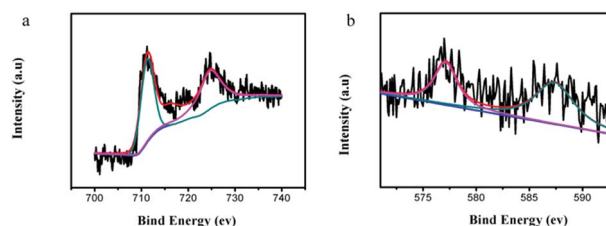


Fig. 6 XPS spectra of 4.0 wt% Cr-doped  $\alpha$ -Fe<sub>2</sub>O<sub>3</sub> nanoparticles (a) Fe 2p, (b) Cr 2p.



operating temperature. It is a common behavior on the surface of  $\alpha$ -Fe<sub>2</sub>O<sub>3</sub> or similar semiconducting metal oxides which can be explained by the kinetics and mechanics of gas adsorption and desorption. When the heating temperature is low, the chemical activation of nanoparticles is accordingly low, and it causes a low response. The increasing temperature leads to positive chemical activation, and the sensor gets the maximum response at a certain heating temperature. The further increasing operating temperature results in some adsorbed gas molecules escaping from surface before gas reaction, and then the response decreases correspondingly.

Meanwhile, Fig. 7a shows that the Cr-doped  $\alpha$ -Fe<sub>2</sub>O<sub>3</sub> gas sensors achieve a maximum sensitivity at 100 °C, while the pure  $\alpha$ -Fe<sub>2</sub>O<sub>3</sub> sensor obtain the maximum sensitivity at 120 °C. The gas responses of the sensors based on the pure, 2.0 wt% 4.0 wt% 6.0 wt% and 8.0 wt% Cr-doped  $\alpha$ -Fe<sub>2</sub>O<sub>3</sub> to 50 ppm H<sub>2</sub>S at 100 °C is 112, 155, 213, 102 and 65, respectively. The result revealed that sensor based on 4.0 wt% Cr-doped  $\alpha$ -Fe<sub>2</sub>O<sub>3</sub> showed the highest response to 50 ppm H<sub>2</sub>S and the value was about two times higher than that of pure  $\alpha$ -Fe<sub>2</sub>O<sub>3</sub>. According to the above test result, we could surmise that the Cr on sensor would play a crucial role in the governing mechanism. Therefore, further measurements were carried out using this specific composition (4 wt%) and operating temperature (100 °C) to explore the effect of other factors on the sensing properties of Cr-doped  $\alpha$ -Fe<sub>2</sub>O<sub>3</sub>.

Subsequently, variations in the electrical conductance were measured on  $\alpha$ -Fe<sub>2</sub>O<sub>3</sub> nanoparticles. Butane, ammonia, ethanol and methane common gases (50 ppm) used as probe molecules to investigate the cross-sensitivity of the sensor at an operating temperature of 100 °C (Fig. 7b). Compared with the conductance change in response to 50 ppm H<sub>2</sub>S at 100 °C, the responses of the 4.0 wt% Cr-doped  $\alpha$ -Fe<sub>2</sub>O<sub>3</sub> sensor to other gases are negligible. The 2.0 wt% Cr-doped  $\alpha$ -Fe<sub>2</sub>O<sub>3</sub> sensor shows a low response to ammonia and ethanol. Consequently, it was concluded that the sensor using as-synthesized 4.0 wt%

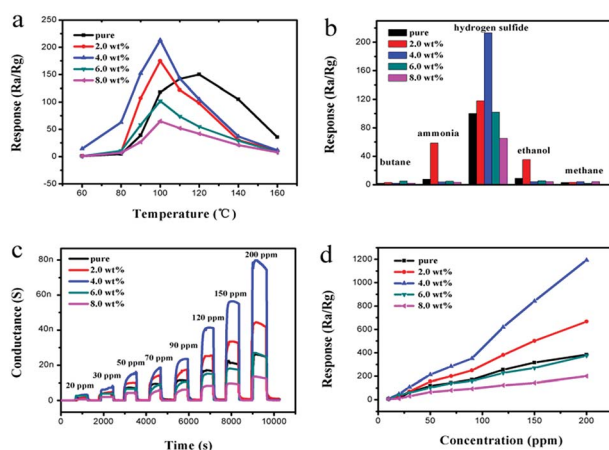


Fig. 7 (a) Gas responses of the sensors based on the pure, 2.0 wt%, 4.0 wt%, 6.0 wt%, and 8.0 wt% Cr-doped  $\alpha$ -Fe<sub>2</sub>O<sub>3</sub> nanoparticles vs. operating temperatures to 50 ppm H<sub>2</sub>S. (b) Gas responses of five sensors to 50 ppm various target gases at 100 °C. (c) Real-time response curves of five sensors to different H<sub>2</sub>S concentration at 100 °C. (d) Gas responses of five sensors as a function of the H<sub>2</sub>S concentration at 100 °C.

Cr-doped  $\alpha$ -Fe<sub>2</sub>O<sub>3</sub> nanoparticles showed excellent selectivity to H<sub>2</sub>S as opposed to other test gases.

The concentrations of hydrogen sulfide were varied from 20 to 200 ppm. Transient response curves of the sensor (composed of pure, 2.0 wt%, 4.0 wt%, 6.0 wt%, and 8.0 wt% Cr-doped  $\alpha$ -Fe<sub>2</sub>O<sub>3</sub>) at the optimal temperature of 100 °C are shown in Fig. 7c. The nearly rectangle-shaped response and recovery curves indicate the excellent hydrogen sulfide response and rapid reaction rate of the sensor. Exposing the sensor to H<sub>2</sub>S significantly increases conductance until it reaches saturation. After the removal of H<sub>2</sub>S, the conductance approaches its initial value.

Fig. 7d shows the relationship between the response of the sensor and H<sub>2</sub>S concentration from 20 to 200 ppm calculated from Fig. 7c. Increasing the concentration accelerates the response. Among them, the response of the sensor based on the 4.0 wt% Cr-doped  $\alpha$ -Fe<sub>2</sub>O<sub>3</sub> was apparently higher than the other sensors. The response of Cr-doped Fe<sub>2</sub>O<sub>3</sub> sensors showed almost no saturation with the variation of H<sub>2</sub>S concentrations between 20 and 200 ppm, indicating a wide response range of the Cr-doped sensor and its possible application in detecting high H<sub>2</sub>S concentration environment.

From these, the Cr doping amount of 4.0 wt% was considered as the optimum doping concentration. Then the response and recovery characteristics of the sensor based on 4.0 wt% Cr-doped  $\alpha$ -Fe<sub>2</sub>O<sub>3</sub> nanoparticles were investigated to 50 ppm hydrogen sulfide gases at 100 °C. As shown in Fig. 8a, the conductance increased upon exposure to hydrogen sulfide gases, which was consistent with the gas sensing behavior of n-type oxide semiconductor. The response and recovery times of the sensors based on the 4.0 wt% Cr-doped  $\alpha$ -Fe<sub>2</sub>O<sub>3</sub> were 29 and 80 s, respectively. Stability of the sensors is also investigated. The 4.0 wt% Cr-doped  $\alpha$ -Fe<sub>2</sub>O<sub>3</sub> sensor was stored in air and kept working at 100 °C for subsequent sensing property tests at a level of 50 ppm H<sub>2</sub>S after aging for 30 days. It can be seen that

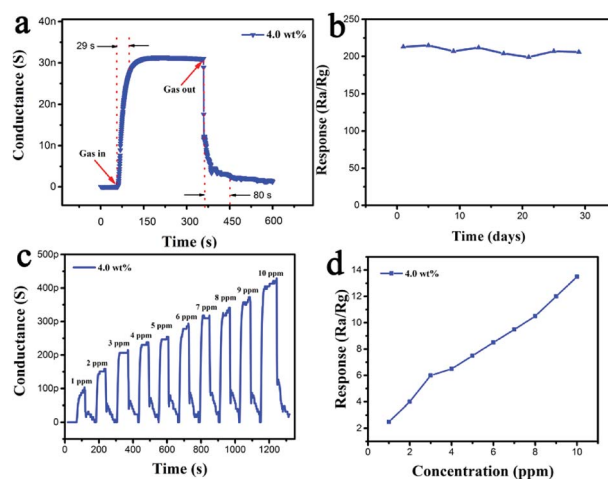


Fig. 8 (a) Dynamic response of the sensor based on 4 wt% Cr-doped  $\alpha$ -Fe<sub>2</sub>O<sub>3</sub> to 50 ppm H<sub>2</sub>S at 100 °C. (b) Stability of the sensor to 50 ppm H<sub>2</sub>S. (c) Dynamic response of the sensors to different concentrations H<sub>2</sub>S from 1 ppm to 10 ppm. (d) Responses of the sensor to different concentrations of H<sub>2</sub>S.



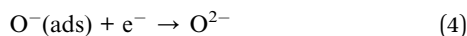
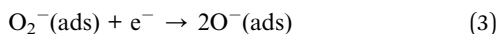
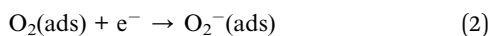
Table 1 Comparison of the sensing performance of Fe<sub>2</sub>O<sub>3</sub> sensors

Material	H <sub>2</sub> S concentration (ppm)	Temperature (°C)	Response	Detection limit (ppm)	Reference
Porous $\alpha$ -Fe <sub>2</sub> O <sub>3</sub>	50	350	66.7	1	12
Ag loaded Fe <sub>2</sub> O <sub>3</sub>	100	160	220	50	8
Pd decorated Fe <sub>2</sub> O <sub>3</sub>	50	160	75	10	10
Au modified Fe <sub>2</sub> O <sub>3</sub>	10	250	6.4	1	9
Fe <sub>2</sub> O <sub>3</sub> @WO <sub>3</sub>	10	150	190	0.5	14
Cr-doped $\alpha$ -Fe <sub>2</sub> O <sub>3</sub>	50	100	213	1	This work

the sensor presented a nearly constant response to H<sub>2</sub>S during the test, showing that the sensor exhibited long-term stability (Fig. 8b). We also investigated the detection limit of H<sub>2</sub>S by the developed sensor. As shown in Fig. 8c, we detected dynamic response curve of sensor based 4 wt% Cr-doped  $\alpha$ -Fe<sub>2</sub>O<sub>3</sub> to H<sub>2</sub>S ranging from 1 ppm to 10 ppm at 100 °C. Fig. 8d showed the relationship between the response of the sensor and H<sub>2</sub>S concentration from 1 to 10 ppm. The detection of 4 wt% Cr-doped  $\alpha$ -Fe<sub>2</sub>O<sub>3</sub> to 1 ppm H<sub>2</sub>S had the responses of about 2.5. When we tested H<sub>2</sub>S below 1 ppm at optimal temperature, the sensor did not have response.

A comparison of the sensing performances between the sensor in this work and other H<sub>2</sub>S sensors based on  $\alpha$ -Fe<sub>2</sub>O<sub>3</sub> reported previously is summarized in Table 1. From the table, comprehensively considering the gas response and operating temperature, it is obvious that 4.0 wt% Cr-doped  $\alpha$ -Fe<sub>2</sub>O<sub>3</sub> nanoparticles showed a high gas response at a low operating temperature. This was conducive to practical application and energy conservation. Therefore, the sensor based on 4.0 wt% Cr-doped  $\alpha$ -Fe<sub>2</sub>O<sub>3</sub> nanoparticles had more superiority than those reported in the literature.

**3.2.2 Gas sensing mechanism.** It is known that metal oxide gas sensing depends on the interaction between the test gas and the adsorbed oxygen species on the surface of the material.<sup>38,39</sup>  $\alpha$ -Fe<sub>2</sub>O<sub>3</sub> is a n-type semiconductor. Therefore, when the  $\alpha$ -Fe<sub>2</sub>O<sub>3</sub> are exposed in an air atmosphere, oxygen molecules will adsorb on the  $\alpha$ -Fe<sub>2</sub>O<sub>3</sub> surface and capture electrons from  $\alpha$ -Fe<sub>2</sub>O<sub>3</sub> to generate the chemisorbed oxygen species at higher temperatures, leading to an increase in resistance. The main chemical equations involved in the process are shown as follows (eqn (1)–(4)):<sup>40,41</sup>



When the  $\alpha$ -Fe<sub>2</sub>O<sub>3</sub> sensor is exposed to H<sub>2</sub>S atmosphere, the surface oxygen ions react with the H<sub>2</sub>S molecule and release a number of electrons back into the semiconductor, resulting in a decrease in resistance of the sensor. This reaction process may be as eqn (5)



However,  $\alpha$ -Fe<sub>2</sub>O<sub>3</sub> presented high catalyst for H<sub>2</sub>S oxidation, and the dominant product was SO<sub>2</sub>. Steijns *et al.* studied the H<sub>2</sub>S oxidation reaction, they showed that the SO<sub>2</sub> formation rate was very slow at low temperatures. It was attributed to the high activation energy of SO<sub>2</sub> formation, which would be about 125 kJ mol<sup>-1</sup>. Whereas the activation energy for sulfur formation was between 8 and 50 kJ mol<sup>-1</sup>. So, Berben *et al.* prepared  $\alpha$ -Fe<sub>2</sub>O<sub>3</sub>-based catalysts, with chromium as additives. It showed good activity and good selectivity, which directly and selectively oxidized H<sub>2</sub>S with O<sub>2</sub> into elemental sulfur.<sup>42,43</sup>

Fig. 9 shows in a double logarithmic plot the variation of the response of  $\alpha$ -Fe<sub>2</sub>O<sub>3</sub> sensor *versus* H<sub>2</sub>S concentration. The linear trend can be related to the conductance model limited by the electron transport across the intergranular Schottky barrier<sup>24,44</sup> where

$$\sigma \propto \exp(-eVs/kT) \quad (6)$$

( $\sigma$  is the conductance and  $eVs$  represents the surface barrier height at the intergranular contact).

According to this model, the response of the  $\alpha$ -Fe<sub>2</sub>O<sub>3</sub> nanoparticles is explained by using the following equation:<sup>45,46</sup>

$$\log \sigma/\sigma_0 = A_g + \beta \log P_g \quad (7)$$

where  $\sigma_0$  denotes the conductance in the absence of the target gas,  $A_g$  is a prefactor,  $P_g$  is the gas partial pressure, and  $\beta$  is the response order. Mechanisms were formulated to describe the

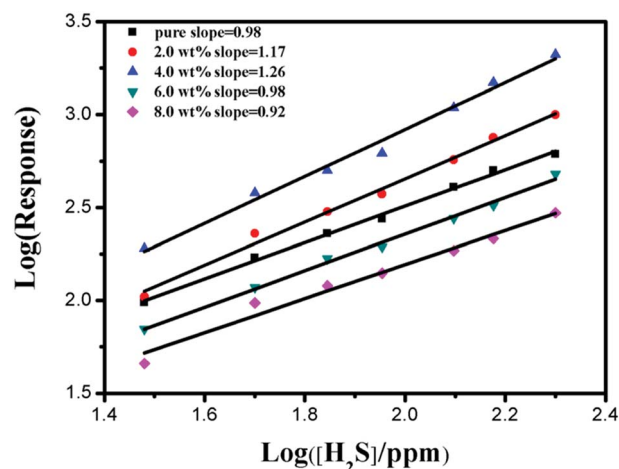


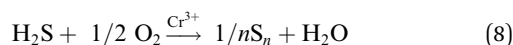
Fig. 9 Response variation for the pure, 2.0 wt%, 4.0 wt%, 6.0 wt% and 8.0 wt% Cr-doped  $\alpha$ -Fe<sub>2</sub>O<sub>3</sub> nanoparticles.



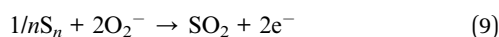
surface reaction and predict the  $\beta$  value in eqn (7). This is usually 1 or 1/2, depending on the charge state of the surface species, the stoichiometry of the elementary surface reactions, and the microstructure of the material. These properties contribute to the fluctuations of the response order value by different weights.

In the case of pristine  $\alpha$ -Fe<sub>2</sub>O<sub>3</sub> nanoparticles (Fig. 9), the calculated  $\beta$  value (*i.e.*, the slope of the curve described by eqn (7)) was about 0.98. Differently, 2.0 and 4.0 wt% Cr-doped  $\alpha$ -Fe<sub>2</sub>O<sub>3</sub> sensors show  $\beta$  values about 1.17 and 1.26. This can be reasonably ascribed to the presence of Cr element which may give rise to a different sensing mechanism at the microscale level.

Therefore, a mechanism was suggested to explain the excellent gas response of Cr-doped  $\alpha$ -Fe<sub>2</sub>O<sub>3</sub>. First, when H<sub>2</sub>S gas flows in, the H<sub>2</sub>S molecules are oxidized into elemental sulfur and H<sub>2</sub>O by the Cr<sup>3+</sup> catalyst in  $\alpha$ -Fe<sub>2</sub>O<sub>3</sub>. The adsorption process is as follows (eqn (8)):



In the meantime, some of the chemisorbed oxygen species reacted with elemental sulfur (eqn (9))



The ability of a reacting species to overcome a free energy barrier that is preventing a reaction is commonly modeled by the Arrhenius equation. For most of the chemical reactions, including the primitive reaction and primitive action, the Arrhenius equation gives the dependence of rates,  $K$ , of a chemical reaction on the absolute temperature  $T$  (in Kelvin) as shown in eqn (10):

$$K = A \exp(-E_a/RT) \quad (10)$$

This equation shows that the rate constant exponentially increases as activation energy ( $E_a$ ) decreases. For the pristine  $\alpha$ -Fe<sub>2</sub>O<sub>3</sub> sensor, higher activation energy is required for produce SO<sub>2</sub>. Therefore, the operating temperature of the reaction is higher. In the presence of Cr<sup>3+</sup>, the  $\alpha$ -Fe<sub>2</sub>O<sub>3</sub> sensor provides a reaction path with lower activation energy, providing a high response at a low temperature. For these reasons, the working temperature of the Cr-doped  $\alpha$ -Fe<sub>2</sub>O<sub>3</sub> sensors can be reduced to low temperature while the sensitivity was still kept high.

Finally, the further increasing of Cr doping content, the size of  $\alpha$ -Fe<sub>2</sub>O<sub>3</sub> gas sensing material became larger and the agglomeration of the nanoparticles became more obvious (Fig. 4d and e), which would reduce surface-to-volume ratio and efficient diffusion of the gas molecules. This may be the reason for the poor performance of 6.0 wt%, and 8.0 wt% Cr-doped  $\alpha$ -Fe<sub>2</sub>O<sub>3</sub> sensors.

## 4. Conclusions

In summary, we have developed a simple one-step hydrothermal method for the synthesis of Cr-doped  $\alpha$ -Fe<sub>2</sub>O<sub>3</sub>

nanoparticles with different doping levels. The results of X-ray diffraction, EDS and XPS data proved that Cr ion successfully entered into the crystal lattice of  $\alpha$ -Fe<sub>2</sub>O<sub>3</sub> without deteriorating the original crystal structure. Furthermore, an appropriate amount of Cr-doped  $\alpha$ -Fe<sub>2</sub>O<sub>3</sub> (4.0 wt% Cr-doped  $\alpha$ -Fe<sub>2</sub>O<sub>3</sub> sensor in this work) display, upon exposure to H<sub>2</sub>S, outstanding sensing properties even at relatively low operating temperature, and the sensitivity resulted as much higher than that of the pristine sensor. This behaviour could be attributed to the nanometer size effect and catalysis effect. Hence, we can confirm that the doping of Cr into  $\alpha$ -Fe<sub>2</sub>O<sub>3</sub> is a promising strategy for improving the gas sensing performance of the  $\alpha$ -Fe<sub>2</sub>O<sub>3</sub> based gas sensor.

## Conflicts of interest

There are no conflicts to declare.

## Acknowledgements

This work was partly supported by the National Natural Science Foundation of China (Grant No. 61574118), and the Key Project of Science and Technology Plan of Fujian Province (Grant No. 2015H0038).

## Notes and references

- 1 C. K. Chan and X. Yao, *Atmos. Environ.*, 2008, **42**, 1–42.
- 2 Y. Zeng, K. Zhang, X. Wang, Y. Sui, B. Zou, W. Zheng and G. Zou, *Sens. Actuators, B*, 2011, **159**, 245–250.
- 3 N. S. Ramgir, P. K. Sharma, N. Datta, M. Kaur, A. K. Debnath, D. K. Aswal and S. K. Gupta, *Sens. Actuators, B*, 2013, **186**, 718–726.
- 4 S. Moon, N. M. Vuong, D. Lee, D. Kim, H. Lee, D. Kim, S.-K. Hong and S.-G. Yoon, *Sens. Actuators, B*, 2016, **222**, 166–172.
- 5 T. Yu, X. Cheng, X. Zhang, L. Sui, Y. Xu, S. Gao, H. Zhao and L. Huo, *J. Mater. Chem. A*, 2015, **3**, 11991–11999.
- 6 K.-H. Kim, E.-C. Jeon, Y.-J. Choi and Y.-S. Koo, *Atmos. Environ.*, 2006, **40**, 4478–4490.
- 7 K.-H. Kim, Y. J. Choi, E. C. Jeon and Y. Sunwoo, *Atmos. Environ.*, 2005, **39**, 1103–1112.
- 8 Y. Wang, Y. Wang, J. Cao, F. Kong, H. Xia, J. Zhang, B. Zhu, S. Wang and S. Wu, *Sens. Actuators, B*, 2008, **131**, 183–189.
- 9 V. Balouria, N. S. Ramgir, A. Singh, A. K. Debnath, A. Mahajan, R. K. Bedi, D. K. Aswal and S. K. Gupta, *Sens. Actuators, B*, 2015, **219**, 125–132.
- 10 Y. Wang, F. Kong, B. Zhu, S. Wang, S. Wu and W. Huang, *Mater. Sci. Eng., B*, 2007, **140**, 98–102.
- 11 Z. Jiang, J. Li, H. Aslan, Q. Li, Y. Li, M. Chen, Y. Huang, J. P. Froning, M. Otyepka, R. Zbořil, F. Besenbacher and M. Dong, *J. Mater. Chem. A*, 2014, **2**, 6714–6717.
- 12 J. Deng, J. Ma, L. Mei, Y. Tang, Y. Chen, T. Lv, Z. Xu and T. Wang, *J. Mater. Chem. A*, 2013, **1**, 12400–12403.
- 13 Z. Sun, H. Yuan, Z. Liu, B. Han and X. Zhang, *Adv. Mater.*, 2005, **17**, 2993–2997.



- 14 L. Yin, D. Chen, M. Feng, L. Ge, D. Yang, Z. Song, B. Fan, R. Zhang and G. Shao, *RSC Adv.*, 2015, **5**, 328–337.
- 15 K.-I. Choi, H.-J. Kim, Y. C. Kang and J.-H. Lee, *Sens. Actuators, B*, 2014, **194**, 371–376.
- 16 G.-J. Sun, S.-W. Choi, A. Katoch, P. Wu and S. S. Kim, *J. Mater. Chem. C*, 2013, **1**, 5454–5462.
- 17 A. B. Bodade, A. B. Bodade, H. G. Wankhade, G. N. Chaudhari and D. C. Kothari, *Talanta*, 2012, **89**, 183–188.
- 18 X. Wang, W. Wang, H. Li, C. Fu, Y. Ke and S. He, *Sens. Actuators, B*, 2012, **169**, 10–16.
- 19 M. K. Verma and V. Gupta, *Sens. Actuators, B*, 2012, **166–167**, 378–385.
- 20 Y. Wang, S. Wang, H. Zhang, X. Gao, J. Yang and L. Wang, *J. Mater. Chem. A*, 2014, **2**, 7935–7943.
- 21 I. Giebelhaus, E. Varechkina, T. Fischer, M. Rumyantseva, V. Ivanov, A. Gaskov, J. R. Morante, J. Arbiol, W. Tyrre and S. Mathur, *J. Mater. Chem. A*, 2013, **1**, 11261–11268.
- 22 S. Bhuvaneshwari and N. Gopalakrishnan, *J. Alloys Compd.*, 2016, **654**, 202–208.
- 23 I. Jiménez, M. A. Centeno, R. Scotti, F. Morazzoni, J. Arbiol, A. Cornet and J. R. Morante, *J. Mater. Chem.*, 2004, **14**, 2412–2420.
- 24 M. D'Arienzo, L. Armelao, C. M. Mari, S. Polizzi, R. Ruffo, R. Scotti and F. Morazzoni, *J. Am. Chem. Soc.*, 2011, **133**, 5296–5304.
- 25 P. Elumalai, J. Zosel, U. Guth and N. Miura, *Ionics*, 2009, **15**, 405–411.
- 26 E. Rossinyol, A. Prim, E. Pellicer, J. Arbiol, F. Hernández-Ramírez, F. Peiró, A. Cornet, J. R. Morante, L. A. Solovyov, B. Tian, T. Bo and D. Zhao, *Adv. Funct. Mater.*, 2007, **17**, 1801–1806.
- 27 L. Wang, A. Teleki, S. E. Pratsinis and P. I. Gouma, *Chem. Mater.*, 2008, **20**, 4794–4796.
- 28 R. K. Sharma, M. C. Bhatnagar and G. L. Sharma, *Sens. Actuators, B*, 1997, **45**, 209–215.
- 29 X. Fu, F. Bei, X. Wang, X. Yang and L. Lu, *J. Raman Spectrosc.*, 2009, **40**, 1290–1295.
- 30 M. F. Hassan, M. M. Rahman, Z. P. Guo, Z. X. Chen and H. K. Liu, *Electrochim. Acta*, 2010, **55**, 5006–5013.
- 31 H. Li, W. Xie, B. Liu, C. Wang, Y. Wang, X. Duan, Q. Li and T. Wang, *Sens. Actuators, B*, 2017, **242**, 404–411.
- 32 S. Y. Lee, D.-H. Kim, S. C. Choi, D.-J. Lee, J. Y. Choi and H.-D. Kim, *Microporous Mesoporous Mater.*, 2014, **194**, 46–51.
- 33 J. Gong, K. Yao, J. Liu, Z. Jiang, X. Chen, X. Wen, E. Mijowska, N. Tian and T. Tang, *J. Mater. Chem. A*, 2013, **1**, 5247–5255.
- 34 N. Li, J. Zhang, Y. Tian, J. Zhao, J. Zhang and W. Zuo, *Chem. Eng. J.*, 2017, **308**, 377–385.
- 35 H. J. Kim, J. W. Yoon, K. I. Choi, H. W. Jang, A. Umar and J. H. Lee, *Nanoscale*, 2013, **5**, 7066–7073.
- 36 S. Shen, J. Jiang, P. Guo, C. X. Kronawitter, S. S. Mao and L. Guo, *Nano Energy*, 2012, **1**, 732–741.
- 37 Y. Wang, B. Liu, S. Xiao, X. Wang, L. Sun, H. Li, W. Xie, Q. Li, Q. Zhang and T. Wang, *ACS Appl. Mater. Interfaces*, 2016, **8**, 9674–9683.
- 38 M. E. Franke, T. J. Koplín and U. Simon, *Small*, 2006, **2**, 36–50.
- 39 M. Tiemann, *Chemistry*, 2007, **13**, 8376–8388.
- 40 Z. Liu, B. Liu, W. Xie, H. Li, R. Zhou, Q. Li and T. Wang, *Sens. Actuators, B*, 2016, **235**, 614–621.
- 41 Y. Wang, B. Liu, S. Xiao, H. Li, L. Wang, D. Cai, D. Wang, Y. Liu, Q. Li and T. Wang, *J. Mater. Chem. A*, 2015, **3**, 1317–1324.
- 42 A. PiÉPlu, O. Saur, J.-C. Lavalley, O. Legendre and C. NÉDez, *Catal. Rev.*, 1998, **40**, 409–450.
- 43 J. A. Rodriguez, M. Pérez, T. Jirsak, L. González, A. Maiti and J. Z. Larese, *J. Phys. Chem. B*, 2001, **105**, 5497–5505.
- 44 C. O. Park and S. A. Akbar, *J. Mater. Sci.*, 2003, **38**, 4611–4637.
- 45 R. W. J. Scott, S. M. Yang, N. Coombs, G. A. Ozin and D. E. Williams, *Adv. Funct. Mater.*, 2003, **13**, 225–231.
- 46 R. W. J. Scott, S. M. Yang, G. Chabanis, N. Coombs, D. E. Williams and G. A. Ozin, *Adv. Mater.*, 2001, **13**, 1468–1472.

